BEHAVIOUR OF LOCALLY DAMAGED Q355 STEEL EQUAL ANGLES SUBJECTED TO COMPRESSION

Song-Yang He [1], Xing Huang [1], Xiang-Yun Liu [1], Zhong Li [1], Tao Gong [1], Hui-Qiang Yan [2, 3] and Shao-Bo Kang [2, 3, *]

[1] Southwest Electric Power Design Institute Co., LTD., China Power Engineering Consulting Group, 16 Dongfeng Road, Chenghua District, Chengdu 610021, China

[2] Key Laboratory of New Technology for Construction of Cities in Mountain Area (Chongqing University), Ministry of Education, Chongqing 400045, China

[3] School of Civil Engineering, Chongqing University, Chongqing 400045, China

* (Corresponding author: E-mail: kang0119@cqu.edu.cn)

ABSTRACT

Steel angles in transmission towers may experience corrosion in the service life due to bad exposure conditions. However, limited experimental results are available about the remaining load capacity of corroded steel angles in compression at present. This paper presents experimental tests, numerical simulations and design method of steel angles with local damages at the mid-height or end induced by corrosion. Five groups of steel angles with different depths of local damages at different locations were tested under axial compression in the experimental programme, and the load capacity and failure mode of steel angles were obtained. Numerical models are developed and validated using test data, and parametric studies are conducted to investigate the influence of depth and slenderness of steel angles on ultimate load. Moreover, design equations are developed for locally damaged steel angles, and comparisons with numerical results show yield reasonably accurate estimations of the ultimate load. Comparisons are also made between the calculated result using the developed equation and existing design curves in the relevant code to demonstrate the effect of local damage on the buckling coefficient of steel angles. It shows that the local damage at the mid-height or the end of steel angles could significantly reduce the buckling coefficient, and therefore, it has to be considered when evaluating the ultimate load of steel angles in transmission towers in service.

1. Introduction

Steel structures may be exposed to local or overall corrosion in the whole service life due to the environmental effects. To evaluate the structural performance after corrosion, experimental tests have been carried out on different types of structural steel and its members. At the material level, studies have been conducted on the residual yield and ultimate strengths of corroded steel plates [1-3]. Design methods have also been proposed in which the effective thickness of steel plates could be used to evaluate the ultimate strength of corroded steel plates [4]. Sarveswaran et al. [5] proposed a computational method to assess the reliability of corroded steel structural components based on interval probability theory.

A wide range of experimental tests and numerical simulations have been conducted to investigate the effect of different types of corrosion on the behaviour of steel beams in bending. Tang et al. [6] and Wang et al. [7] measured the geometric characteristics of corroded high-performance steel beams exposed to different environments using three-dimensional scanning technology and studied the effects of corrosion on the flexural behaviour of the beam. They found that existing design method could predict the flexural capacity of corroded beams conservatively. Peng et al. [8], Zhang et al. [9] and Chai et al. [10], Liu and Zhang [11], and Zhao et al. [12, 13] systematically investigated the influences of location and ratio of corrosion on the moment resistance, buckling and fatigue behaviour of steel beams in bending and concluded that local corrosion had a greater impact on the flexural stiffness of beams compared to overall corrosion. Moreover, design equations were also developed based on experimental results to quantify the moment capacity of corroded steel beams. Sheng et al. [14] also derived design equations to evaluate the yield load and ultimate load of rusted H-beams. Based on monotonic tensile tests on corroded steel beams, Xu et al. [15] obtained the time-dependent failure probability and reliability index of corroded steel beams using the theory of probability density evolution. Under reversed cyclic loading conditions, Wang et al. [16] proposed the skeleton curve and restoring force model, which could be used to describe the seismic performance of corroded steel frames.

With regard to steel columns, existing research mainly focused on the load capacity in compression after corrosion. Toledo et al. [17] established the correlation between residual compressive strength and the severity of corrosion through experiments and numerical modelling. They proposed an evaluation equation for residual compressive strength using corrosion damage volume as a reduction factor. Wang et al. [18] conducted quasi-static tests on seven H-shaped steel columns exposed to atmospheric corrosion. They observed a correlation between the cyclic hardening parameter of corroded steel and the yield-to-tensile strength difference, suggesting the possibility of premature cracking in different loading stages of corroded columns. Hussain et al. [19]

proposed a new design method for the plastic failure and stability analysis of single angle members, which simplified the calculation equations for single angle member in design codes. Zhang et al. [20, 21], Zheng et al. [22] and Nie et al. [23] studied the seismic performance of corroded steel columns and proposed a method to predict the ultimate strength of the column under lateral cyclic loading. Xu et al. [1] investigated the failure modes, lateral load-carrying capacity, ductility, and energy dissipation performance of H-shaped steel columns through low-cycle fatigue tests. Even though experimental and numerical investigations have been widely performed on the ultimate load capacity and failure mode of corroded steel columns, there is still a lack of study on the compressive behaviour of steel angles with corrosion, including the buckling resistance and failure mode. Abdelrahman et al. [24] investigated the flexural-torsional buckling behaviour of eccentrically loaded members and established the effective stress-strain relationship for single angle members through finite element and multiple regression analyses.

This paper presents experimental and numerical studies on the compressive behaviour of steel angles with simulated local damages induced by corrosion at the mid-height or end. In the experimental programme, five groups of steel angles with local damages in different regions were tested in compression, and the load capacity and failure mode of the angle were obtained and compared to show the influences of the location and depth of local damage on compression behaviour. Numerical models were also established and validated against test data, and were then used for parametric studies on the influence of the slenderness of steel angles on load resistance. Finally, design equations were developed in accordance with experimental and numerical results which could be used to quantify the ultimate load of steel angles with local damages.

2. Experimental programme

2.1. Specimen design

Steel equal angles L125×8 mm with a width of 125 mm and a thickness of 8 mm were used in the experimental programme, as shown in Fig. 1. According to field observations of transmission towers in service, two different locations of local damage were determined, namely, either at the mid-height of steel angles or at the end. A simplified processing method was also adopted to produce the local damage instead of corrosion. In the method, a local damage with a length of 260 mm along the height of steel angles was made by grinding the outer face of the steel angles to a certain depth. Oszvald et al. [25] employed a mechanical milling process method to simulate corrosion by representing it as a reduction in thickness. The study established a correlation between the degree of thickness reduction and the failure modes exhibited by the specimens. Furthermore, based on the prospective behaviour pattern of b/t, the remaining

load-carrying capacity of specimens could be predicted. The author also developed design equations to calculate the remaining load-carrying capacity of compressed steel angles. Note that the two legs of each steel angle were ground to simulate the local damage induced by corrosion, whereas the depth of the local damage varied from 1 mm to 2 mm, as listed in Table 1. Huang et al. [26] investigated towers in different regions with the service life ranging from 25 to 40 years and found that the net thickness of the most severely corroded steel angles was 6.41 mm (with the nominal thickness of 8 mm), while at the tower base, the net thickness of the most severely corroded diagonal angles was only 2.18 mm (with the nominal thickness of 5 mm). Therefore, in this study, a corrosion thickness of 1 to 2 mm was chosen to investigate the corrosion range of commonly used steel angles. Thus, a total of five groups of steel angles were tested in axial compression, including one group of steel angles without damage, two groups with local damage of different depths at the mid-height, and two groups with local damage of different depths at the end. The length of steel angles was kept at 1150 mm, but pin supports were connected to both ends of each steel angle using five bolts on each leg, so that axial compression could be applied to the steel angle. Accordingly, the slenderness of steel angle about the weakest axis was fixed at 50. Table 1 includes the parameters of steel angles. In the designation of steel angles, DCN represents the specimen without local damage, DC-M1 and DC-M2 denote steel angles with 1 mm and 2 mm deep local damages at the mid-height, respectively, and DC-E1 and DC-E2 stand for the specimens with 1 mm and 2 mm deep local damages at the end.
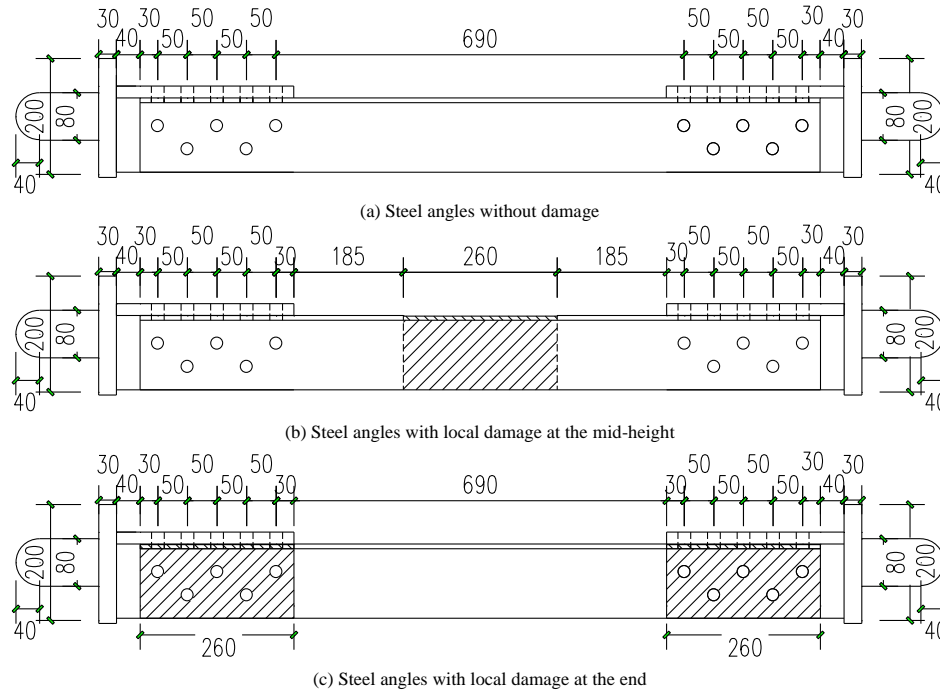

(a) Steel angles without damage

(b) Steel angles with local damage at the mid-height

(c) Steel angles with local damage at the end

**Fig. 1** Details of steel angles in the experimental programme

Table 1
Parameters of steel angles in the experimental programme

| Steel angles	Cross-section (mm)	Damage	Location of damage	Geometry of local damage (mm)	Length (mm)
DCN	L125×8	No damage	--	--	1150
DC-M1	L125×8	Both legs	Mid-height	L=260mm, t=1mm	1150
DC-M2	L125×8	Both legs	Mid-height	L=260mm, t=2mm	1150
DC-E1	L125×8	Both legs	End	L=260mm, t=1mm	1150
DC-E2	L125×8	Both legs	End	L=260mm, t=2mm	1150

2.2. Tension tests on steel plates

Fig. 2(a) shows the dimension of steel coupons used in tension tests. The gauge length of steel coupons was 83.8 mm, in which the width of steel was kept at mm. The thickness of steel coupons remained the same as steel angles, namely, 8 mm. Three samples were cut from steel angles along the length and tested in tension. Fig. 2(b) shows the tensile stress-strain curve of coupons. It can be observed from the figure that steel coupons developed elastic stage, yield plateau, hardening stage, and finally necking before fracture. The average yield strength of coupons was 391.4 MPa, and the ultimate tensile strength was 573.7 MPa.
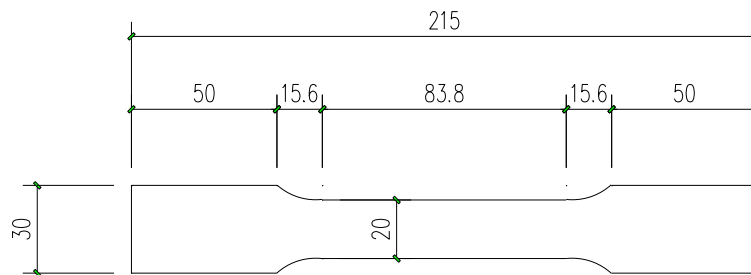
(a) Geometry and dimensions of steel coupons
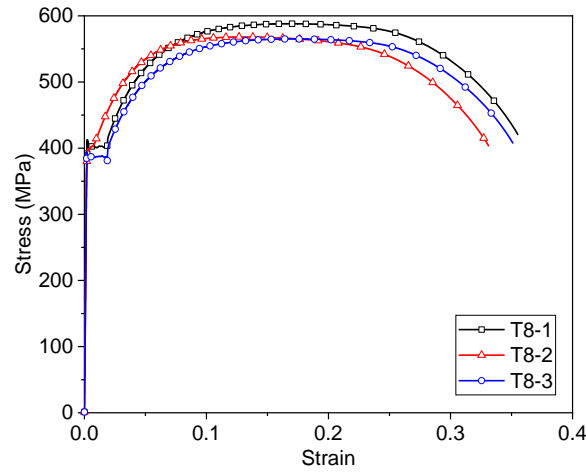
(b) Stress-strain curves of steel plates

Fig. 2 Typical stress-strain curve of steel angles in tension

2.3. Test setup and loading procedures

After the installation of pin supports at both ends of steel angles, an axial compression was applied to the steel angle by using a hydraulic compression machine, as shown in Fig. 3(a). Note that the applied load was in alignment with the centroid of the steel angles and was measured by a load cell. The lateral

deflections of steel angles were recorded through linear variable displacement transducers parallel to the legs, as shown in Fig. 3(b). Besides, strain gauges were also attached to the face of steel angles to measure the longitudinal strain (see Figs. 3(b, c and d)). Three sections along the height of steel angles were selected to mount strain gauges, namely, the mid-height and both ends of steel angles.
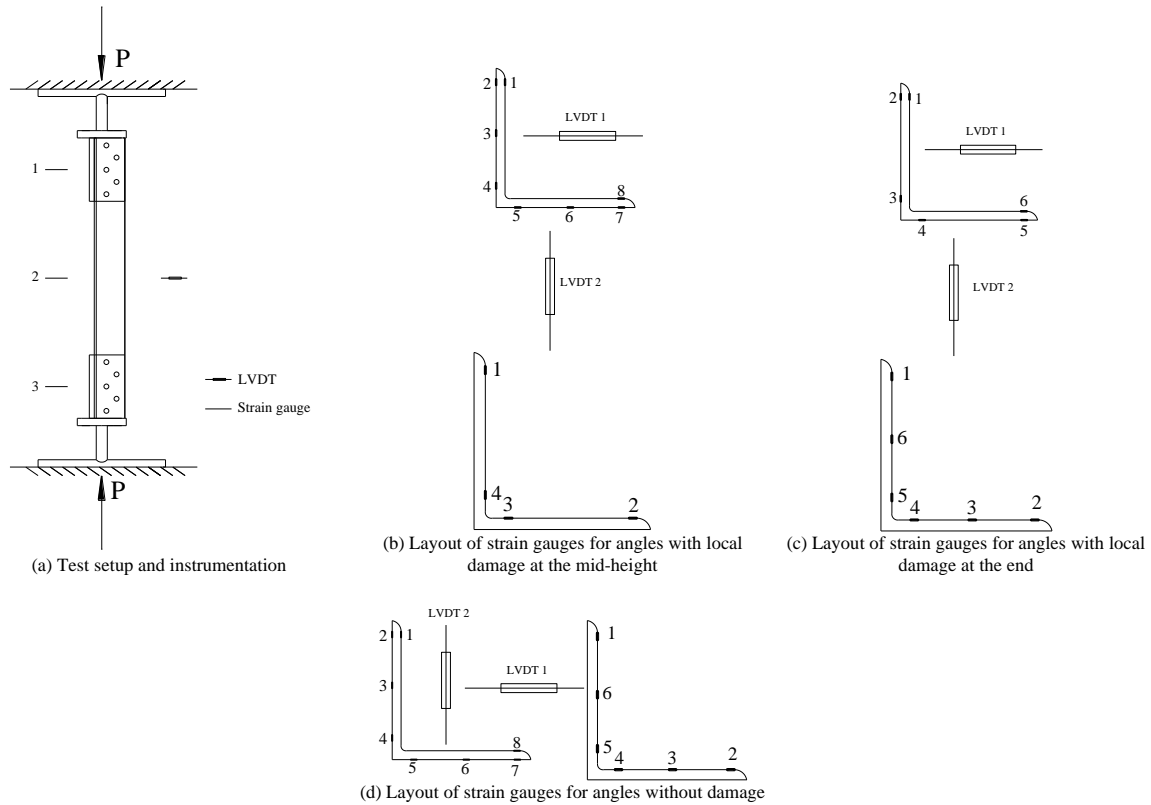

(a) Test setup and instrumentation

(b) Layout of strain gauges for angles with local damage at the mid-height

(c) Layout of strain gauges for angles with local damage at the end

(d) Layout of strain gauges for angles without damage

Fig. 3 Schematic view of test setup and instrumentation

3. Experimental tests and discussions

3.1. Load-deflection curves

Fig. 4 shows the load-deflection curve of steel angle DCN without local damage. Note that deflections perpendicular to the two legs were measured using LVDTs. It can be observed from the figure that steel angles started to deflect with increasing axial compression, but the deflections measured in the two directions differed greatly from each other due to the presence of initial

imperfections. The lateral deflection increased gradually until the ultimate load was reached. Following the attainment of the peak load, the lateral deflection increased rapidly with decreasing load, indicating the failure of steel angles. The final failure of the steel angles was induced by global buckling in which bending and twisting were combined. The ultimate load of the steel angle was 441.0 kN, corresponding to a mid-height deflection of 6.7 mm. It should be pointed out that the deflection of DCN-1 in direction 2 decreased before the attainment of the ultimate load, possibly as a result of the twisting of the steel angle during global buckling.
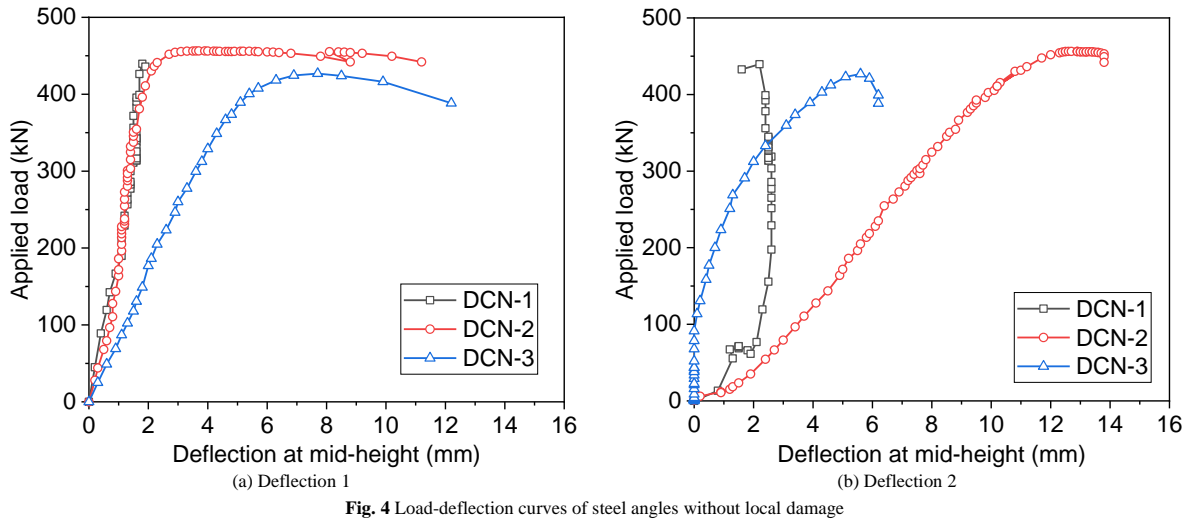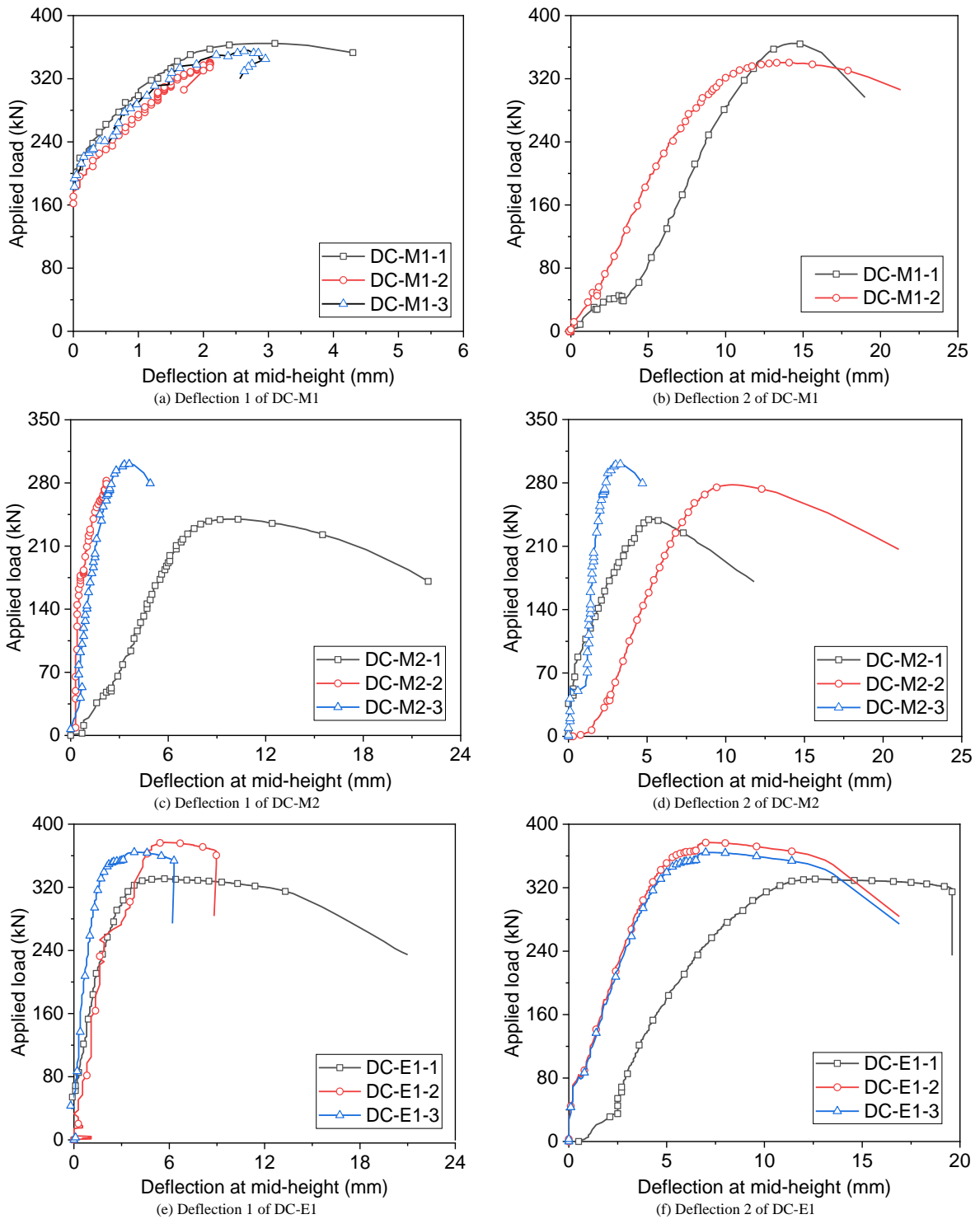
(a) Deflection 1

(b) Deflection 2

Fig. 4 Load-deflection curves of steel angles without local damage

(a) Deflection 1 of DC-M1

(b) Deflection 2 of DC-M1

(c) Deflection 1 of DC-M2

(d) Deflection 2 of DC-M2

(e) Deflection 1 of DC-E1

(f) Deflection 2 of DC-E1
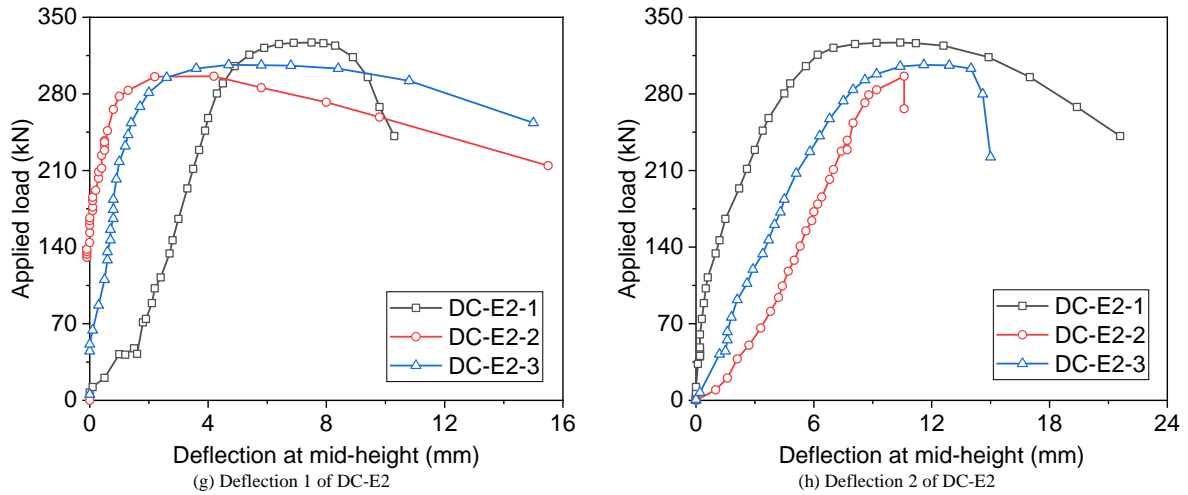
(g) Deflection 1 of DC-E2

(h) Deflection 2 of DC-E2

Fig. 5 Load-deflection curves of steel angles with local damage

Fig. 5 shows the load-deflection curves of steel angles with different depths of damage at different regions. It can be observed that locally damaged steel angles began to deflect with the increase in the applied load, and the lateral deflection at the mid-height increased slowly until the ultimate load of steel angles was reached. However, apparent differences existed in the overall trend of load-deflection curves in the two directions, as shown in Figs. 5(a and b), which might be related to the different angles of bending and twisting when local buckling occurred in the locally damaged region. Comparisons among load-deflection curves of steel angles suggested that the ultimate load of steel angles with different depths of local damage differed greatly from each other. The ultimate load of DC-M1 with a 1 mm deep local damage was 353.7 kN, whereas that of DC-M2 was reduced by 18.8% to only 287.1 kN with the depth of local damage was increased to 2 mm (see Figs. 5(c and d)). Therefore, the ultimate load of steel angles decreased significantly with the increase of the depth of local damage at the mid-height.

When the local damage was located at the end of steel angles, similar load-deflection curves were obtained for DC-E1, as shown in Figs. 5(e and f). The ultimate load of DC-E1 was 347.7 kN, close to that of DC-M1, indicating that the location of damage did not have a significant effect on the ultimate load of steel angles when the depth of the local damage was only 1 mm. If the depth of local damage at the end was increased to 2 mm, the ultimate load of steel angle DC-E2 was reduced to 310.4 kN, around 11.7% lower than that of DC-E1. However, when compared with DC-M2, the ultimate load of DC-E2 was

roughly 8.1% higher, indicating that a deeper local damage near the end of steel angles did not decrease the ultimate load of steel angles as much as that at the mid-height did.

3.2. Failure modes of steel angles

Fig. 6 shows the typical failure modes of steel angles under axial compression. It can be observed that overall buckling occurred in the steel angle without local damage (see Fig. 6(a)). The steel angle mainly developed significant lateral deflections at the initial stage of loading. Once the applied load reached the peak value, the lateral deflection increased rapidly, and the steel angle exhibited twisting. However, in addition to overall deflections, local buckling in the locally damaged region was also observed with regard to steel angles with local damage, as shown in Figs. 6(b-e). For instance, steel angles DC-M1 and DC-M2 with local damage at the mid-height showed local buckling in the proximity of the mid-height. Similar failure modes were also observed near the end of steel angles DC-E1 and DC-E2. It is observed that the undamaged steel angle experienced overall buckling. However, in the case of locally damaged steel angles, the local damage significantly reduced the resistance at that specific location. During the compression process, the affected location could develop localised buckling failure due to the increased width-to-thickness ratio.
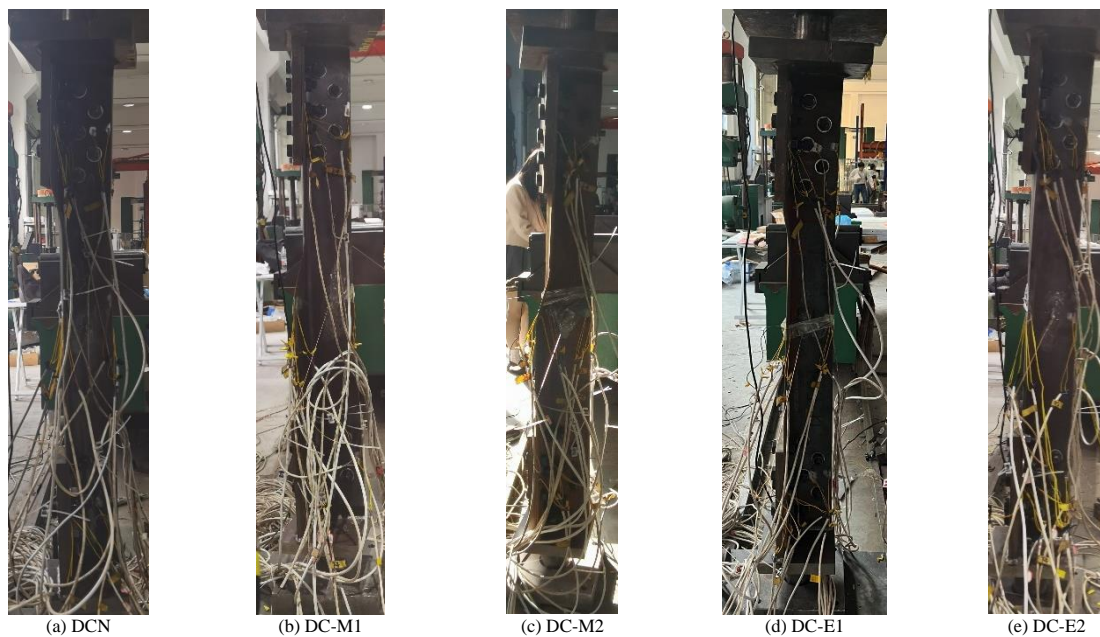

(a) DCN   (b) DC-M1   (c) DC-M2   (d) DC-E1   (e) DC-E2

Fig. 6 Typical failure modes of steel angles in compression

3.3. Discussions on test results

Fig. 10 shows the effect of local damage depth on the ultimate load of steel angles under axial compression. Test results showed that the ultimate load of the undamaged steel angle DCN was 441.7 kN. When a local damage of 1 mm

depth was produced at the mid-height, the ultimate load was reduced to by 20.0% to 353.7 kN, and the value was further decreased to 287.1 kN if the local damage depth was increased to 2 mm. When the local damage was located at the end of steel angles, similar conclusions could be obtained when comparisons were made between the undamaged and damaged steel angles, as shown in Fig. 10.

It is noteworthy that when the local damage depth was 1 mm, the ultimate loads of steel angles with local damages at the mid-height and end remained rather close to each other. Nevertheless, if the depth of local damage was increased to 2 mm, the ultimate load of steel angles with damaged end was 310.4 kN, considerably greater than that with the local damage at the mid-height. Hence, when the depth of local damage was 2 mm, it was more detrimental to the ultimate load of steel angles when it is located at the mid-height compared with that at the end.

3.4. Load-strain curves

Fig. 7 shows the load-strain relationship of steel angles under axial compression. It can be observed that steel angle DCN without local damage developed different longitudinal strain at the mid-height and the end. The measured strain at the mid-height increased with the increasing axial compression, as shown in Fig. 7(a). Nonetheless, the compressive strain of M4 and M5 was significantly smaller than that of M8 and M9 due to the bending of the steel angles about the minor axis. When the axial load approached the ultimate load, the strain of M4 and M5 gradually changed from compressive strain to tensile strain, but that of M8 and M9 increased rapidly with the increasing axial compression. Note that the maximum strain associated with the load capacity had exceeded the yield strain of steel angles, indicating that the steel angle failed at the inelastic stage. Different variations of steel strains were measured at the end of steel angles, as shown in Fig. 7(b). Strains E1 and E2 at one toe of the angles were compressive and increased rapidly with the

increasing load. However, strains E5 and E6 at the other toe were rather close to zero in the whole loading process. Moreover, the peak compressive strain corresponding to the load capacity was much smaller than the yield strain.
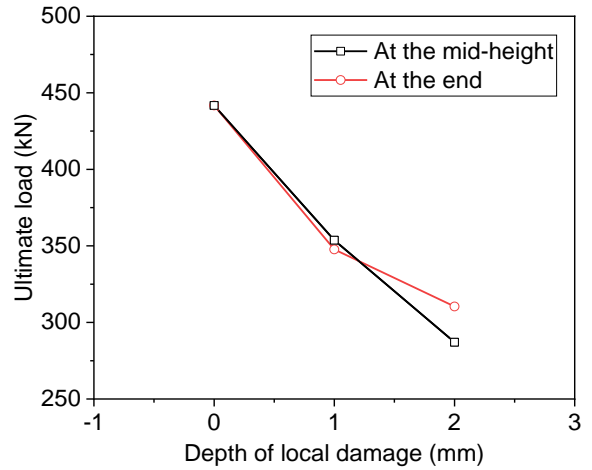

Fig. 10 Effect of local damage on load capacity of steel angles

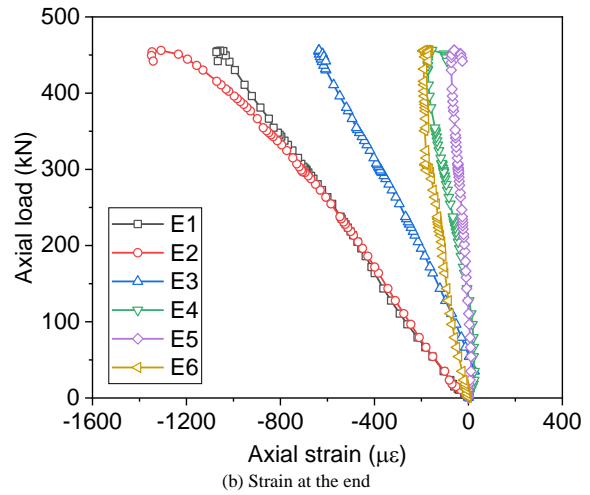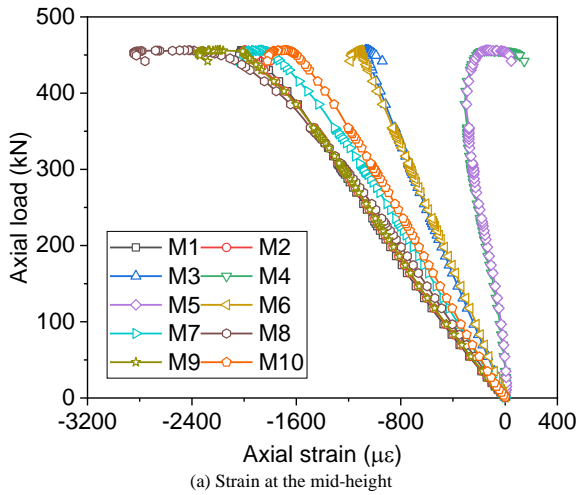(a) Strain at the mid-height

(b) Strain at the end

Fig. 7 Longitudinal strains measured at different sections of steel angle DCN

When the steel angle was produced with a 2 mm deep local damage at the mid-height, most of the measured strains varied similarly to those of DCN, as shown in Fig. 8(a). Special attention should be paid to strains M6 and M7 at the mid-height. During failure of the steel angle, the measured strains M6 and M7

changed their signs from compression to tension, indicating the local buckling of the angle at the mid-height accompanying the overall buckling. As for the strain measured at the end of the steel angle, it was in general similar to that of DCN, as shown in Fig. 8(b).
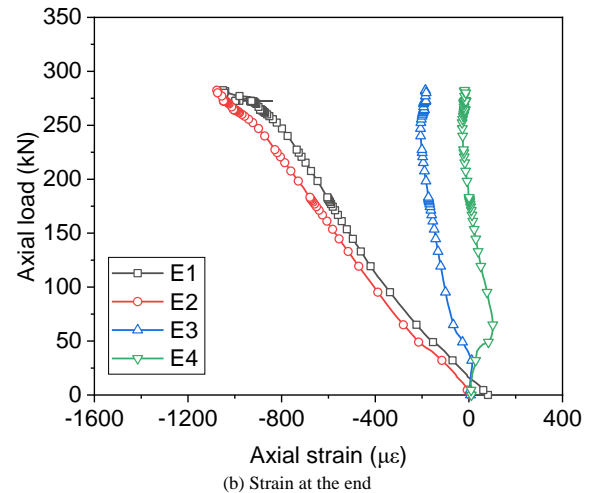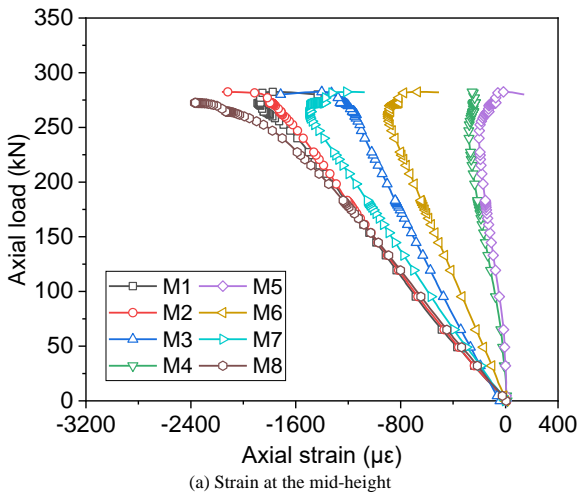

(a) Strain at the mid-height

(b) Strain at the end

Fig. 8 Longitudinal strains measured at different sections of steel angle DC-M2

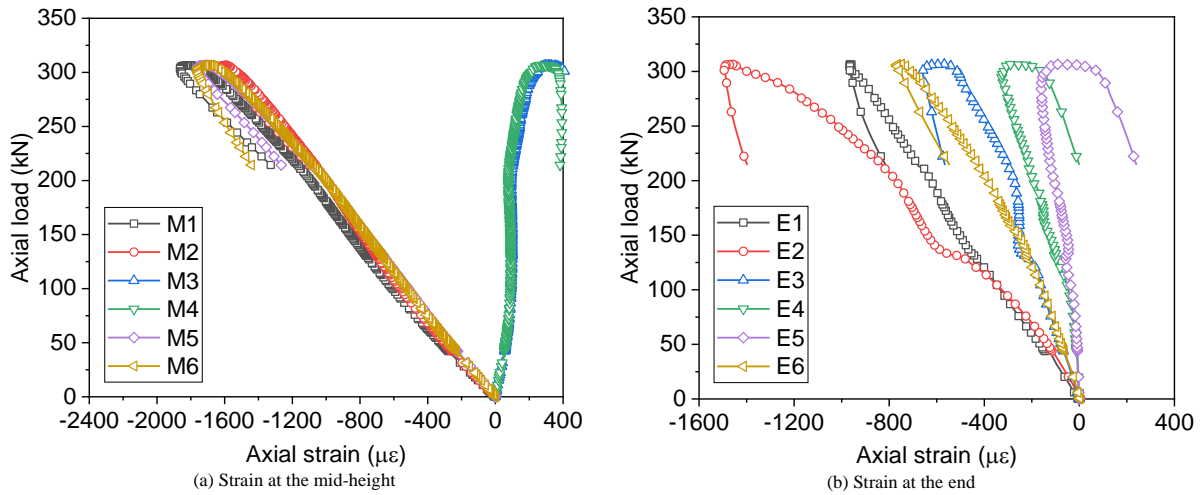(a) Strain at the mid-height (b) Strain at the end

Fig. 9 Longitudinal strains measured at different sections of steel angle DC-E2

When a 2 mm deep local damage was produced at the end, the load-strain curve of steel angle DC-E2 differed greatly from that of undamaged steel angles, as shown in Fig. 9. The strain of M3 and M4 was tensile immediately after loading (see Fig. 9(a)). This phenomenon was induced by the local deformation near the locally damaged region which eventually developed local buckling. The measured tensile strain by M3 and M4 decreased during loading, and then increased rapidly when the ultimate load was reached. Note that strain gauges M1 through M4 measured compressive strains in the whole loading process, and the maximum compressive strain measured at the ultimate load was still considerably smaller than the yield strain. Thus, the locally damage region was at the elastic stage when the steel angle failed. The measured strain at the end of steel angles was in general similar to that at the mid-height, as shown in Fig. 9(b), but the strain of E4 and E5 was compressive rather than tensile at the end.

4. Numerical modelling of steel angles

4.1. Establishment of numerical models

Besides experimental tests, numerical modelling is also performed using ABAQUS [27] to investigate the behaviour of locally damaged steel angles under axial compression. Fig. 11 shows the numerical model for steel angles. In the numerical model, solid element C3D8R is used to model the steel angle and the end plate. The local damage at the mid-height and the end is modelled by reducing the thickness of the steel angle. To simplify the model, steel bolts connecting the steel angle and the end plate are neglected, and the two parts are tied together. Two reference points are defined at both ends of each steel angle to simulate the pin support. Before simulations, the mesh size is properly selected so that it will not affect the accuracy of the numerical model. The mesh size is determined to be 2 mm in the thickness direction and 10 mm along the height of steel angles.
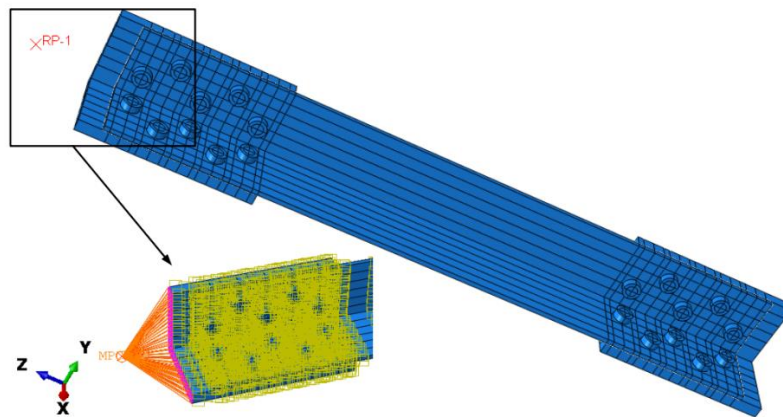

Fig. 11 Numerical models for steel angles under axial compression

Table 2
Comparison between numerical and experimental ultimate loads

Steel angles	Experimental value of ultimate load (kN)	Numerical value of ultimate load (kN)	Numerical value/experimental value
DCN	441.0	427.5	0.97
DC-M1	353.7	340.5	0.96
DC-M2	287.1	289.6	1.00
DC-E1	357.4	362.8	1.02
DC-E2	310.4	331.1	1.07
Average value			1.00
Coefficient of variation			4.3%

### 4.2. Material properties and initial imperfections

The average mechanical properties of steel plates measured through tension tests are adopted in the numerical model. To simplify the stress-strain curve, a bilinear stress-strain curve is employed, of which the elastic modulus remains the same as that measured in the tension tests, and the hardening modulus is calculated as the slope of the stress-strain curve between the yield and ultimate stresses. In addition to the mechanical properties, residual stresses in steel angles are also defined in the numerical model, and the distribution of residual stress across the section is taken from GB 50017-2017 [28]. Initial geometric imperfections are also considered. In most design codes, the initial bending of steel members is assumed to be 1/1000 of the height. This value is also used in the present study.

4.3. Model validation

Table 2 summarises the comparisons between numerical and experimental ultimate loads of locally damaged steel angles under axial compression. It can

be observed from the table that the numerical results are in good agreement with the experimental results. The average ratio of numerical to experimental results is 1.00, with a coefficient of variation of 4.3%. Therefore, the numerical model is capable of predicting the ultimate load of steel angles with good accuracy. In addition to the ultimate load, the load-deflection curve of steel angles can also be predicted with reasonably good accuracy using the numerical model. Fig. 12 shows the comparison between numerical and experimental load-deflection curve of steel angles. Differences exist at the initial stage of loading. The numerical load-deflection curve in general overestimate the initial stiffness of steel angles, as the gap between steel angles and bolts at the top and bottom ends is not considered in the numerical model. In addition, the steel angles might have certain initial deformations or geometric defects, resulting in uncertainty in the location of the largest deflection. However, the presence of gaps between bolts and holes does not significantly affect the ultimate load. When the ultimate load is reached, the numerical deflection increases rapidly with decreasing load.
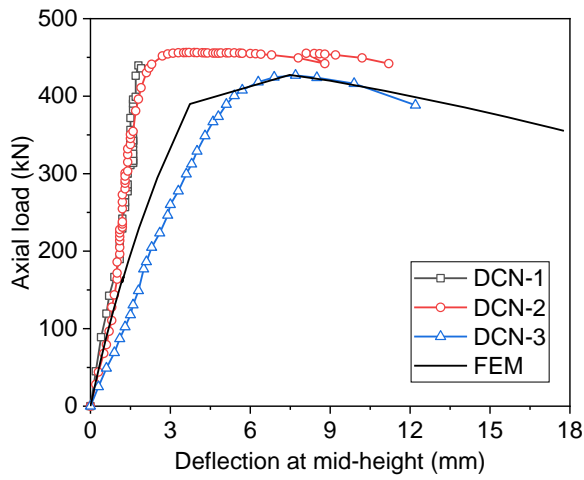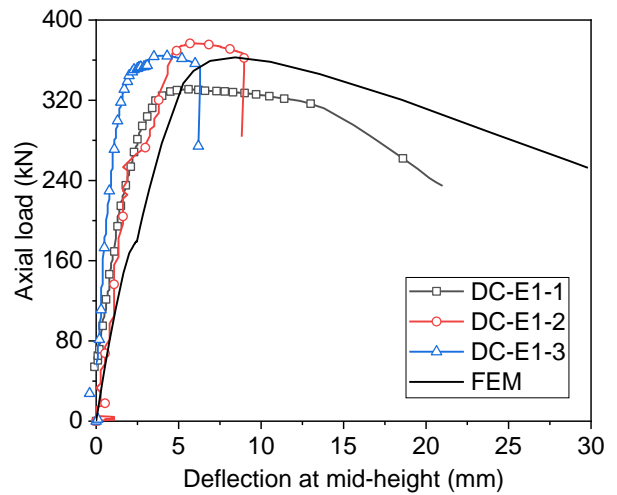

(a) DCN
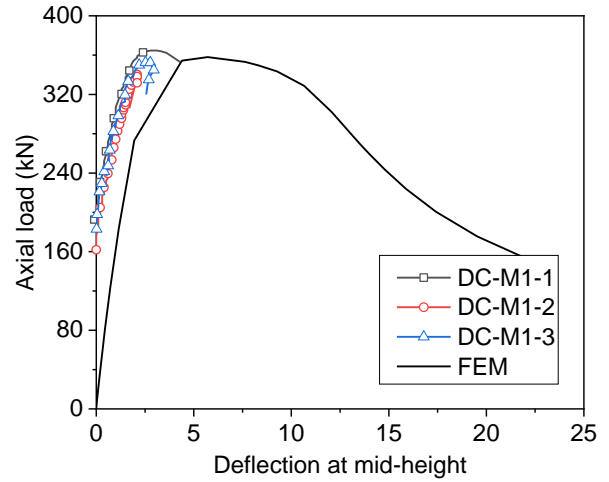
(b) DC-M1 ((mm) should be added to the x axis)
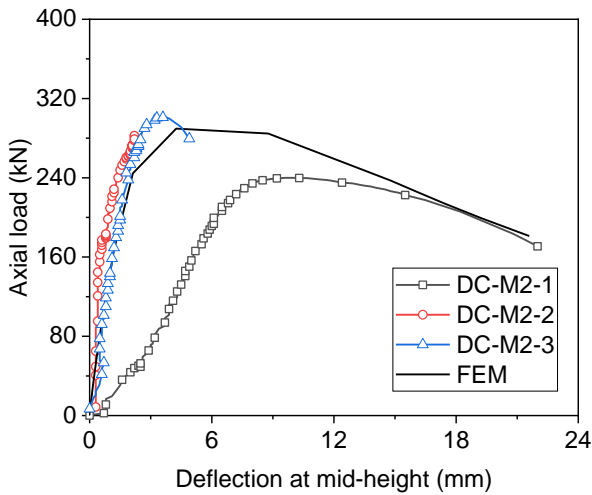
(c) DC-M2

(d) DC-E1
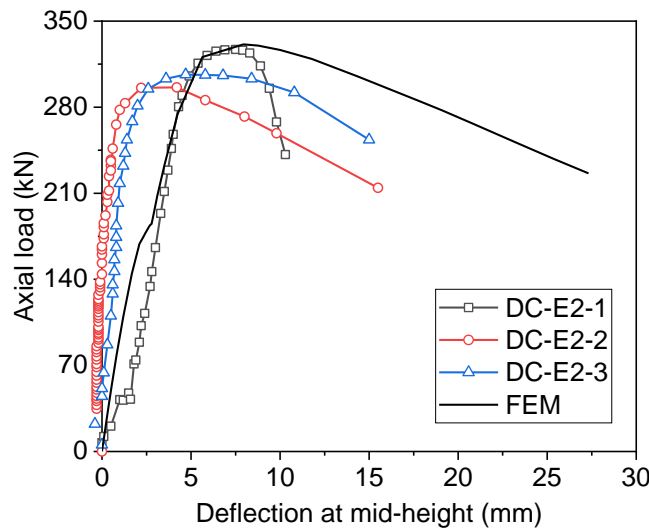
(e) DC-E2

Fig. 12 Comparisons between experimental and numerical load-deflection curves of steel angles

Fig. 13 shows the failure mode of steel angles using numerical simulations. Global buckling of the undamaged steel angle DCN can be observed in Fig. 13(a). The maximum deflection of the steel angle occurs at the mid-height due to the local deformation near the mid-height. The maximum stress appears at

the angle toe and has exceeded the yield strength of steel angles. When local damage is produced at the mid-height, stress concentration in the damaged region can be observed, as shown in Figs. 13(b and c). Eventually, local buckling of steel angles also takes place in the damaged region, leading to the significantly greater Mises stresses. It can be seen that the maximum stress of DC-M1 in the mid-span is 471.0 MPa, whereas that of DC-M2 is 467.7 MPa, indicating that the maximum stress is not significantly affected by the depth of local damage. However, the Mises stress in steel angles with local damage at

the mid-height is also increased as compared with that in the undamaged steel angle. By contrast, when the end of steel angles is damaged, the region with the maximum Mises stress gradually moves towards the end, as shown in Figs. 13(d and e). The maximum local deformation of DC-E1 still occurs at the mid-height, whereas that of DC-E2 appears at the end of the steel angle. Note that the numerical deformation profile of DC-E1 is different from the experimental observation, as in the numerical model the steel angles and the end plate are tied together which prevents the development of local deformation near the end.
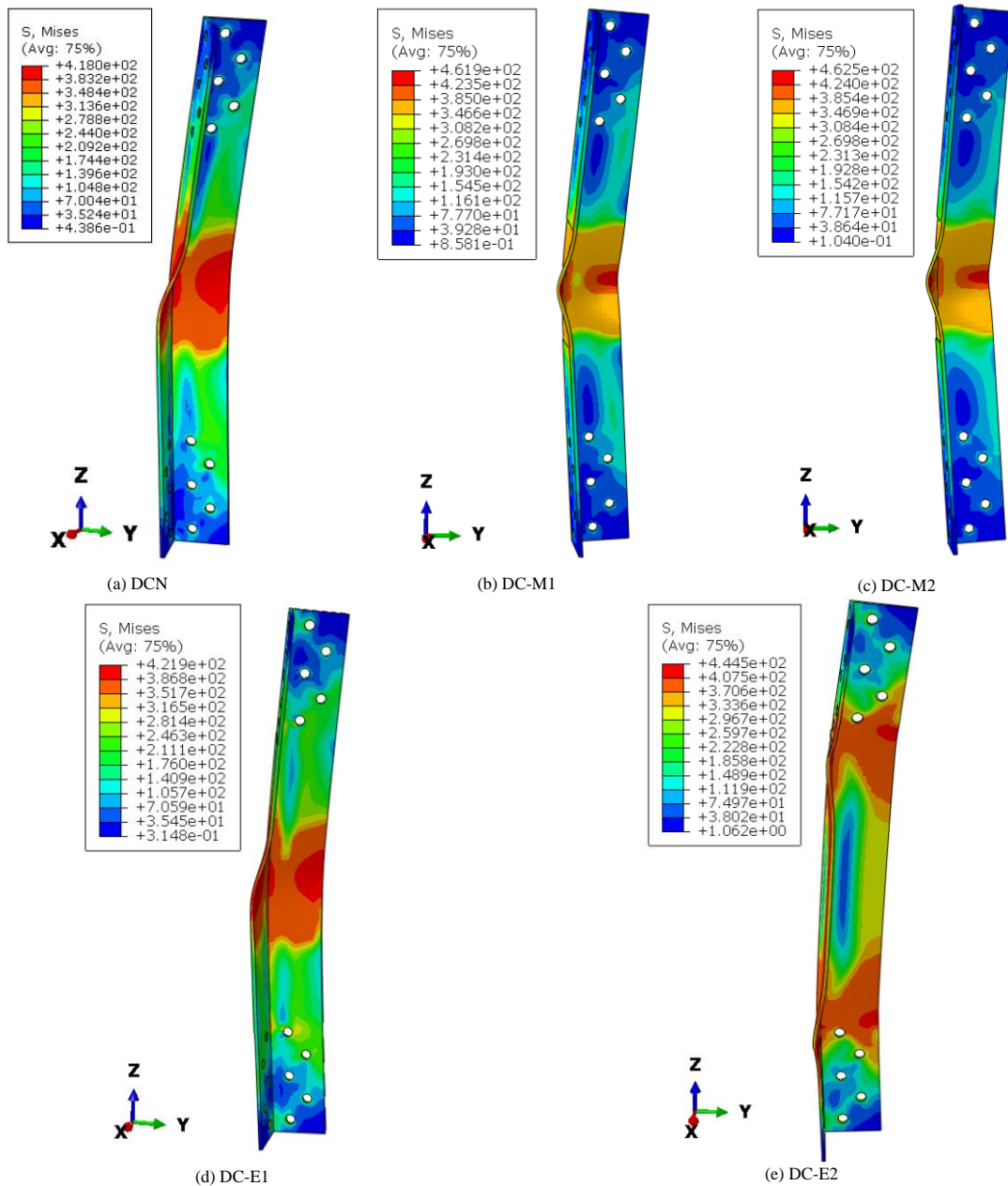

(a) DCN   (b) DC-M1   (c) DC-M2

(d) DC-E1   (e) DC-E2

Fig. 13 Numerical failure modes of steel angles with damages

5. Parametric study

With the verified numerical model, a series of parametric study was conducted to investigate the effects of slenderness and local damage depth on the ultimate load of damaged steel angles, as shown in Figs. 14 and 15. The three aspect ratios are intended to compare the effects of local damage depth and slenderness on the ultimate load-carrying capacity of specimens. The selection of these three aspect ratios is found to reveal underlying patterns during the analysis. Detailed analyses and discussions can be found in the following section.

5.1. Effect of slenderness

Fig. 14 shows the effect of slenderness on the ultimate load of damaged steel angles subjected to axial compression. It can be observed that when the local damage is located at the mid-height of steel angles, the ultimate load decreases almost linearly with increasing slenderness from 50 to 100 (see Fig.

14(a)). For instance, for a damage depth of 1 mm, the ultimate load of steel angles with a slenderness of 50 is 340.5 kN, whereas that of steel angles is reduced to 209.1 kN when the slenderness is increased from 50 to 100. When the damage depth is increased to 2 mm, a similar load-slenderness relationship is obtained for damaged steel angles. However, the slope of the curve is significantly reduced in comparison with the curve of steel angles with 1 mm deep local damage. It indicates that when the damage depth is increased from 1 mm to 2 mm, the effect of slenderness becomes less significant. Fig. 14(b) shows the ultimate load-slenderness relationship when the local damage is located at the end of steel angles. The overall relationship remains similar to those with the local damage at the mid-height. However, it should be pointed out that when the slenderness of steel angles exceeds 50, the ultimate load of steel angles with 1 mm deep local damage is rather close to that with 2 mm deep local damage. It is attributed to the fact that with increasing slenderness, buckling of steel angles dominates in which the local damage at the end plays a limited part.
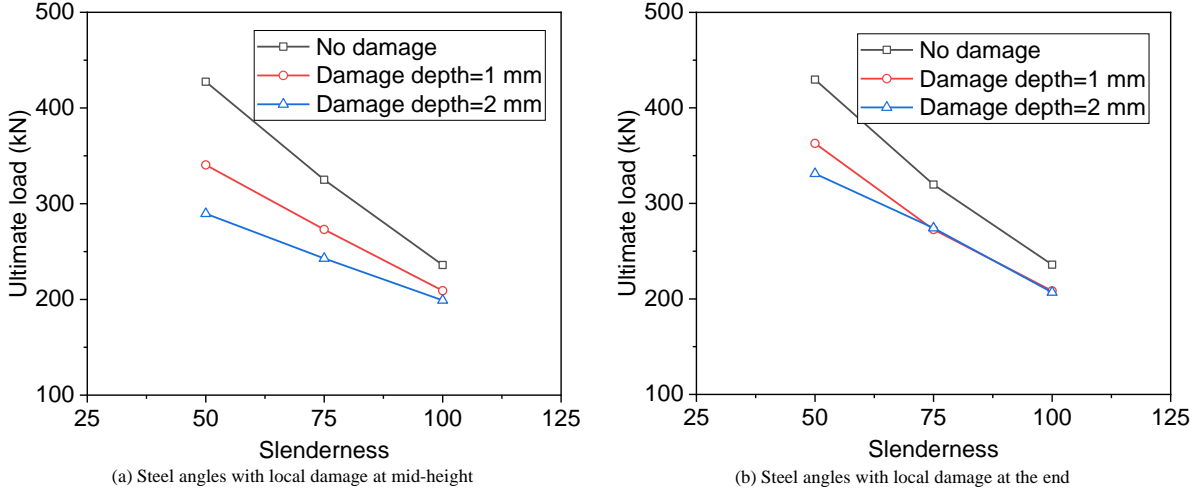
(a) Steel angles with local damage at mid-height

(b) Steel angles with local damage at the end

Fig. 14 Effect of slenderness on load capacity of steel angles

5.2. *Effect of local damage depth*

Fig. 15 shows the effect of local damage depth on the ultimate load of steel angles. It can be observed that for a given slenderness of steel angles, the ultimate load of steel angles decreases significantly with increasing depth of local damage at the mid-height (see Fig. 15(a)). For steel angles with a slenderness of 50, the ultimate load of the undamaged angle was 427.5 kN, whereas that of steel angles with a 2 mm deep local damage was reduced by 32.3% to 289.6 kN. Nonetheless, the reduction of ultimate load with increasing local damage depth becomes less significant when the slenderness of steel angles was increased from 50 to 100. Fig. 15(b) shows the effect of local damage depth on the ultimate load of steel angles when the local damage is located at the end. In general, the ultimate load of steel angles decreases gradually with the increase of the depth of local damage at the end when the slenderness of steel angles is 50. The ultimate load of steel angles with 2 mm deep local damage is 331.1 kN, 23.5% lower than that of the undamaged member. Nevertheless, when the slenderness of steel angles is 75 or 100, the effect of local damage depth on the ultimate load becomes less significant, in particular when the damage depth at the end is increased from 1 mm to 2 mm. Therefore, it can be concluded that local damages at the end of steel angles mainly affect the ultimate load of steel angles with smaller slendernesses.
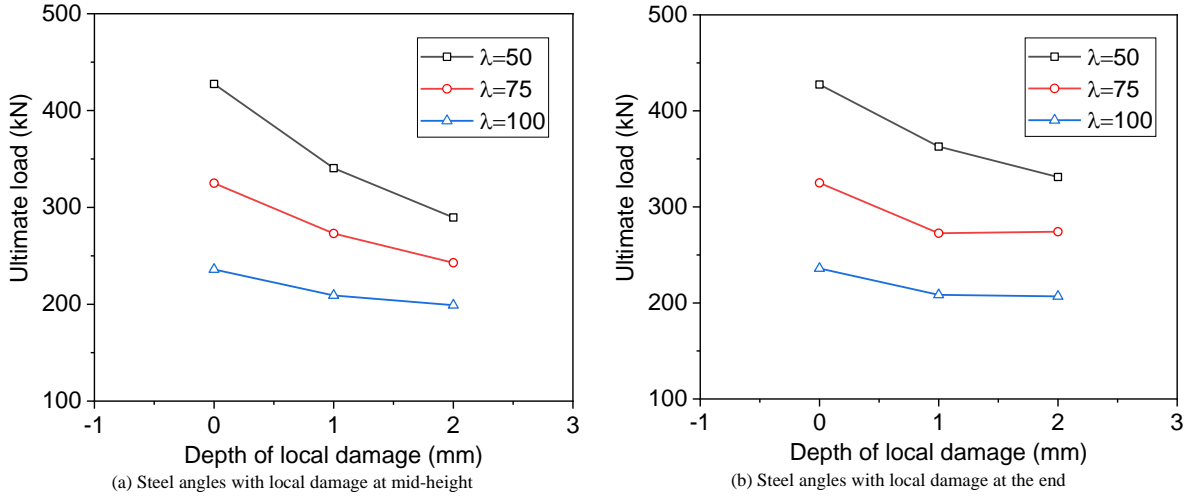

(a) Steel angles with local damage at mid-height

(b) Steel angles with local damage at the end

Fig. 15 Effect of damage depth on load capacity of steel angles

6. Design equations for steel angles

Existing design methods [29] can calculate the ultimate load or the buckling coefficient of steel angles under axial compression, but the effect of local damage at different locations cannot be considered in the design method. In this section, a set of design equations is proposed to take account of the effect of local damage on the global buckling resistance of steel angles. In the equation, the ultimate load of steel angles with local damage can be computed from

$$F = (1 - R\eta_s)F_c \qquad (1)$$

in which F_c is the ultimate load of steel angles without local damage, η_s is the local damage ratio, R is a reduction factor for the slenderness of steel angles, and F is the load capacity of locally damaged steel angles.

For steel angles with different depths of local damage, the local damage ratio is expressed in Eq. (2).

$$\eta_s = \frac{x_z}{t} \qquad (2)$$

$$x_z = \frac{(1-DOV)\times(2Bt-t^2)+t^2-2Bt}{2t-4B} \qquad (3)$$

$$DOV = \frac{V_{dam}}{V_{total}} \qquad (4)$$

where x_z is the equivalent thickness of steel angles after considering the effect of local damage, t is the original thickness of steel angles, B is the original width of steel angles, DOV is the volumetric ratio of the local damage to the whole steel angle, V_{dam} is the volume of the local damage, and V_{total} is the volume of the whole steel angle.

Additionally, the width-to-thickness ratio is a crucial parameter influencing the stability of structural components. Within the limit of the width-to-thickness ratio for equal-leg steel angle, a parametric study of the design equation suggests that b/t may influence x_z (the equivalent thickness of steel angles) and subsequently affect the load-carrying capacity after corrosion. Through the simplification of x_z, it is determined that x_z is the product of DOV and t/2. Therefore, x_z is independent of b/t, indicating that b/t does not affect the proposed design equation.
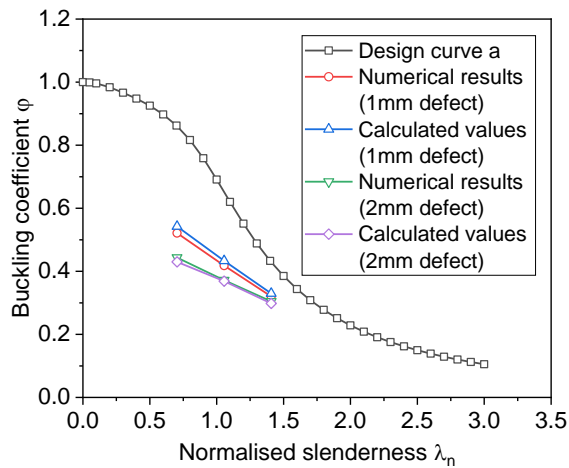
Experimental and numerical results show that the effect of local damage on the load capacity is relevant to the slenderness of steel angles. The effect is more significant when the slenderness of steel angles is small. To determine the influence of slenderness, expressions are developed through linear regression for the reduction factor of slenderness, as expressed in Eqs. (5) and (6).
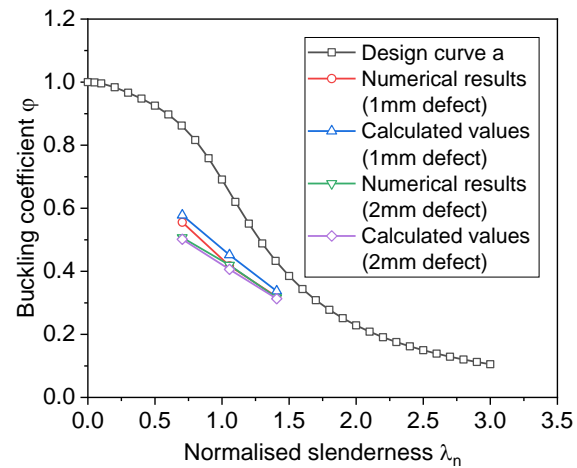
$$R = -0.03071\lambda + 4.65523 \tag{5}$$

$$R = -0.00916\lambda + 1.52063 \tag{6}$$

in which λ is the slenderness of steel angles about the weakest axis.

Fig. 16 shows the comparison of the calculated buckling coefficient using the proposed equations with numerical results and the design curve. The buckling coefficient and normalised slenderness can be determined from Eqs. (7) and (8). It can be observed that the calculated result is in good agreement with the numerical result, but both the calculated and numerical buckling coefficients of steel angles with local damage at the mid-height are far below the design curve, as shown in Fig. 16(a), in particular when the normalised slenderness is small. The difference between the calculated result and the design curve is reduced with increasing normalised slenderness. Besides, the depth of

local damage also has a significant influence on the calculated buckling coefficient. When the depth of local damage is 1 mm at the mid-height, the calculated result is around 35.0% lower than the design curve. When the depth of local damage is increased to 2 mm, the calculated buckling coefficient is further reduced by 41.5% as compared with the design curve.

$$\varphi = \frac{F}{Fc} \tag{7}$$

$$\lambda_n = \frac{\lambda}{\pi} \times \sqrt{\frac{f_y}{E}} \tag{8}$$

where φ is the buckling coefficient, λ_n is the normalised slenderness, f_y is the yield strength of steel angles, and E is the elastic modulus of steel angles.

(a) Local damage at the mid-height   (b) Local damage at the end

Fig. 16 Comparisons between calculated buckling coefficient and design curve of steel angles with local damages

Fig. 16(b) shows the comparison of the calculated buckling coefficient using the proposed equation with the numerical result and design curve. It can be found that the calculated result agrees reasonably well with the numerical result, whereas both of them fall far below the design curve. When the local damage depth is 1 mm, the calculated buckling coefficient is roughly 33.8% lower than the design curve. If the local damage depth is increased to 2 mm, the calculated buckling coefficient becomes 35.8% smaller than the design curve. Furthermore, comparisons can also be made between the calculated buckling coefficient of steel angles with local damage at the mid-height and the end. In general, the local damage at the mid-height will have a more significant influence on the buckling coefficient than that at the end of steel angles. Therefore, in the design process, considerations should be taken to the impact of corrosion on the ultimate compressive load-bearing capacity of steel angles.

7. Conclusions

This paper presents experimental and numerical investigations on the compression behaviour of locally damaged steel angles with equal legs. Five groups of steel angles were tested under axial compression, in which local damages of different depths were prefabricated at different locations. The load resistance and failure pattern of steel angles were obtained through experimental tests. Besides, numerical models were also established for steel angles. Parametric studies were also conducted using the verified numerical model to investigate the influence of local damage depth and slenderness on the ultimate load of steel angles. Finally, design equations were developed to take account of the effect of local damages on ultimate resistance. The following conclusions could be drawn from experimental and numerical studies.

(1) When local damages were located at the mid-height of steel angles, the ultimate resistance of the angle decreased with increasing depth of local damages. The ultimate load of the undamaged steel angle DCN was 441.7 kN, whereas those of steel angles DC-M1 and DC-M2 with 1 mm and 2 mm deep local damages were 353.7 kN and 287.1 kN, respectively, reduced by 19.9% and 35.0% as compared with DCN.

(2) For steel angles with local damages at the end, the ultimate resistance also decreased when the depth of local damages increased from 0 to 2 mm. The ultimate loads of damaged steel angles DC-E1 and DC-E2 were 357.4 kN and 310.4 kN, respectively, roughly 19.1% and 29.7% lower than that of DCN.

(3) Numerical results showed that the influence of local damages on the ultimate load becomes increasingly insignificant when the slenderness of steel angles is increased from 50 to 75. For instance, when the slenderness of steel

angles is 120, a 2.0 deep local damage at the mid-height will only reduce the ultimate load of the steel angle by 15.6% from 235.9 kN to 199.0 kN compared with the undamaged steel angle.

(4) A design method is proposed based on the experimental and numerical results of locally damaged steel angles. In the method, the effect of local damage is considered by converting it to equivalent overall reduction of the steel angle thickness, and a reduction factor is defined to reflect the influence of slenderness on the buckling coefficient of locally damaged steel angles.

References

[1] S.H. Xu, Z.X. Zhang, G.C. Qin, Study on the seismic performance of corroded H-shaped steel columns, Engineering Structures 191 (2019) 39-61.

[2] Y. Sharifi, S. Tohidi, J.K. Paik, Ultimate compressive strength of deteriorated steel web plate with pitting and uniform corrosion wastage, Sci. Iran. 23(2) (2016) 486-499.

[3] A. Cinitha, P.K. Umesha, N.R. Iyer, An overview of corrosion and experimental studies on corroded mild steel compression members, KSCE Journal of Civil Engineering 18(6) (2014) 1735-1744.

[4] T. Kaita, J. Appuhamy, K. Itogawa, M. Ohga, K. Fujii, Experimental Study on Remaining Strength Estimation of Corroded Wide Steel Plates under Tensile Force, 12th East Asia-Pacific Conference on Structural Engineering and Construction (EASEC), Hong Kong, PEOPLES R CHINA, 2011.

[5] V. Sarveswaran, J.W. Smith, D.I. Blockley, Reliability of corrosion-damaged steel structures using interval probability theory, Structural Safety 20(3) (1998) 237-255.

[6] H. Tang, J.X. Peng, C.S. Cai, D.D.K. Lee, Test, 3D Scanning and FE Study on Flexural Behavior of Q550E HPS Beams Subjected to Local Corrosion at Mid-Span Region, International Journal of Steel Structures 22(5) (2022) 1452-1473.

[7] Y.D. Wang, S.H. Xu, A.B. Li, Flexural performance evaluation of corroded steel beams based on 3D corrosion morphology, Structure and Infrastructure Engineering 16(11) (2020) 1562-1577.

[8] J. Peng, L. Xiao, J. Zhang, C.S. Cai, L. Wang, Flexural behavior of corroded HPS beams, Engineering Structures 195 (2019) 274-287.

[9] Z.X. Zhang, S.H. Xu, H. Wang, B.A. Nie, C. Su, Flexural buckling behavior of corroded hot-rolled H-section steel beams, Engineering Structures 229 (2021).

[10] Y. Chai, J.X. Peng, L.F. Xiao, X.H. Liu, J.R. Zhang, Fatigue Behavior of High-Performance Steel Beams Subjected to Different Corrosion Conditions, International Journal of Steel Structures 23(4) (2023) 1105-1118.

[11] X.H. Liu, J.R. Zhang, Experimental Study on Effect of Corrosion on Flexural Load-carrying Capacity of Q550E High-performance Steel Girder, Zhongguo Gonglu Xuebao/China Journal of Highway and Transport 32(11) (2019) 184-191and201.

[12] Z.W. Zhao, S.J. Mo, Q.Q. Xiong, H.Q. Liu, B. Liang, Moment capacity of H-section steel beam with randomly located pitting corrosion, Probabilistic Engineering Mechanics 66 (2021).

[13] Z.W. Zhao, L.M. Tang, N. Zhang, Q. Cai, S.J. Mo, B. Liang, Shear capacity of H-shaped steel beam with randomly located pitting corrosion, Applied Ocean Research 115 (2021).

[14] J. Sheng, J.W. Xia, H.F. Chang, Bending Behavior of Corroded H-Shaped Steel Beam in Underground Environment, Appl. Sci.-Basel 11(3) (2021).

[15] S. Xu, B. Nie, H. Zhang, Time-dependent Reliability Analysis of Corroded Steel Beam Based on Probability Density Evolution Theory, Hunan Daxue Xuebao/Journal of Hunan University Natural Sciences 47(7) (2020) 75-83.

[16] B. Wang, W.Z. Huang, S.S. Zheng, Study on Restoring Force Performance of Corrosion Damage Steel Frame Beams under Acid Atmosphere, Applied Sciences-Basel 9(1) (2019).

[17] K.K. Toledo, H.S. Kim, Y.S. Jeong, I.T. Kim, Residual Compressive Strength of Short Tubular Steel Columns with Artificially Fabricated Local Corrosion Damage, Materials 13(4) (2020).

[18] Y.D. Wang, T. Shi, B. Nie, H. Wang, S.H. Xu, Seismic performance of steel columns corroded in general atmosphere, Steel and Composite Structures 40(2) (2021) 217-241.

[19] A. Hussain, Y.-P. Liu, S.-L. Chan, Finite Element Modeling and Design of Single Angle Member Under Bi-axial Bending, Structures 16 (2018) 373-389.

[20] Q. Zhang, J.N. Wen, Q. Han, Z.F. Wang, J.B. Sun, Seismic performance evaluation of steel circular hollow section bridge piers with corroded ends, Bulletin of Earthquake Engineering (2023).

[21] Z.X. Zhang, S.H. Xu, B. Nie, R. Li, Z. Xing, Experimental and numerical investigation of corroded steel columns subjected to in-plane compression and bending, Thin-Walled Structures 151 (2020).

[22] S.S. Zheng, X.H. Zhang, X.R. Zhao, Experimental investigation on seismic performance of corroded steel columns in offshore atmospheric environment, Structural Design of Tall and Special Buildings 28(4) (2019).

[23] B. Nie, S.H. Xu, H.J. Zhang, Z.X. Zhang, Experimental and numerical studies on the behaviour of corroded cold-formed steel columns, Steel and Composite Structures 35(5) (2020) 611-625.

[24] Z.-L.D. A.H.A. Abdelrahman, Yao-Peng Liu, S.-L.C. ∗ Stability design of single angle member using effective stress-strain method, Structures 20 298-308.

[25] K. Oszvald, P. Tomka, L. Dunai, The remaining load-bearing capacity of corroded steel angle compression members, Journal of Constructional Steel Research 120 (2016) 188-198.

[26] Y. Huang, Z.G. Su, B.R. Zhu, Y.X. Chen, T. Wan, Z.X. Tuo, The influence of corrosion on the bearing capacity characteristics of overhead transmission line tower, Nonferrous Metals Science and Engineering(2023) 1-11.

[27] ABAQUS, Analysis user's manual version 6.13, ABAQUS Inc2013.

[28] Standard for design of steel structures (GB50017-2017), Standards Press of China, Beijing, 2017(in Chinese).

[29] M. Chen, W. Fang, H. Huang, Static behavior of corroded concrete-filled steel tubular members by simulating acid rain solution, Engineering Mechanics 37(2) (2020) 34-43.